RESEARCH ARTICLE

Key Points:
- Large magnitude triggering is rare
- Systematic global increase not observed

Correspondence to:
C. W. Johnson,
cwj@seismo.berkeley.edu

Rare dynamic triggering of remote $M \geq 5.5$ earthquakes from global catalog analysis

Christopher W. Johnson[1], Roland Bürgmann[1], and Fred F. Pollitz[2]

[1]Berkeley Seismological Laboratory and Department of Earth and Planetary Science, University of California, Berkeley, California, USA, [2]U.S. Geological Survey, Menlo Park, California, USA

Abstract Probing the effects of a transient stress on the timing of an earthquake occurrence is necessary for understanding the remote interaction of large-magnitude events. Global catalog data containing 35 years of $M \geq 5.5$ earthquakes allow us to explore for periods of enhanced or suppressed seismic activity. We consider 113 $M \geq 7.5$ main shocks between 1977 and 2012 and focus on seismic activity on time scales from seconds to days following these main shocks. We search for evidence of dynamic triggering of large-magnitude events similar to the previously observed global increase during the first few days following the 2012 M8.6 Indian Ocean main shock. We restrict the analysis to regions of elevated strain during the passage of surface waves. Using a threshold of 0.1 microstrain (~3 kPa) and a temporal window of ±1 year, we stack daily seismicity rate curves using the exclusion-zone declustered $M \geq 5.5$ catalog events in order to resolve deviations from the background rate. Our results do not indicate a significant change in activity for at least 10 days when considering the collective set of 113 main shocks and subsets at M8.0 and M8.5 thresholds. The results also do not indicate immediate triggering of $M \geq 5.5$ events. We do find two instances of increased seismicity in the elevated strain region within 10 days. These increases are subsequent to two main shocks, the 1977 M8.3 and 2012 M8.6, both located in the Indian Ocean. We conclude that a global change in $M \geq 5.5$ earthquake rates following a transient stress from distant earthquakes is a rare occurrence.

1. Introduction

The phenomenon of triggered earthquakes provides insight into the state of stress on a fault prior to nucleation and the conditions required for rupture initiation. Studies of earthquake triggering involve spatiotemporal characterization of known stress perturbations and the associated seismic activity at various distances from a main shock. In the near field, the region within 2–3 fault lengths of the rupture, static stress changes from a fault offset induce aftershock sequences that correlate in space and time with the stress perturbation [*Freed*, 2005; *Harris*, 1998]. Within this near-field aftershock zone, a static stress transfer of 10 kPa or more is found to promote or suppress aftershock sequences, which can include large earthquakes, thereby altering the time to failure in the earthquake cycle [*Reasenberg and Simpson*, 1992; *Stein*, 1999]. Complementing the near-field static stress change is the dynamic stress perturbation during the passage of seismic waves [*Harris and Archuleta*, 1991; *Rybicki et al.*, 1985; *van der Elst and Brodsky*, 2010]. Investigations into the effect of a strong dynamic pulse of energy in combination with the static stress change show that near-field aftershock sequences are enhanced by dynamic triggering [*Parsons*, 2002; *Pollitz and Johnston*, 2006]. One method to separate the effect of static and dynamic stress perturbations is to consider remote earthquakes at distances of negligible static stress changes [*Felzer and Brodsky*, 2005; *Kato et al.*, 2013; *Richards-Dinger et al.*, 2010; *van der Elst and Brodsky*, 2010]. Conversely dynamic stress shadows defined as quiescent periods at remote distances are possible following a transient stress [*Parsons*, 2005; *Pollitz et al.*, 2014].

Widespread recognition of dynamically triggered earthquakes began after the 1992 M7.3 Landers earthquake in Southern California triggered earthquake sequences at distances more than 1250 km from the epicenter, with many of these locations associated with geothermal or volcanic activity [*Gomberg and Bodin*, 1994; *Hill et al.*, 1993]. *Brodsky et al.* [2000] found evidence for dynamic triggering in nonvolcanic regions following the 1999 M7.4 Izmit, Turkey earthquake. Continued efforts have shown that at remote distances, beyond 2–3 fault lengths, transient stresses have the potential to immediately trigger microearthquakes ($M < 3.5$) as well as nonvolcanic tremor during or soon after the passage of seismic waves [*Aiken et al.*, 2013; *Brodsky and Prejean*, 2005; *Gomberg et al.*, 2004; *Peng et al.*, 2010, 2011; *Prejean et al.*, 2004; *Velasco et al.*, 2008]. Dynamic stress levels found to trigger microseismicity and nonvolcanic tremor are on the order 1–10 kPa [*Peng et al.*, 2009;

Tape et al., 2013]. These low-magnitude events and nonvolcanic tremor often occur during the passage of the long-period surface waves and can go undetected in sparsely monitored regions. Less frequently, triggering of earthquakes ranging from $3 < M < 5$ is detected during the passage of the surface wave [*Hill and Prejean*, 2007; *Husker and Brodsky*, 2004; *Pankow et al.*, 2004; *Tape et al.*, 2013]. Other studies have also observed delayed dynamic triggering; i.e., a temporal gap between a transient stress and an increase in remote seismic activity initiating hours to days after the stress perturbation and persisting for time period up to 2 weeks [*Pankow et al.*, 2004; *Peng et al.*, 2011; *Pollitz et al.*, 2012]. *Velasco et al.* [2008] performed a systematic global search of waveform data and detected a significant increase in microseismicity for ~0.8 h following the surface wave arrival from 15 remote $M > 7.0$ earthquakes. Their results are restricted to regions with broadband monitoring capabilities but independent of tectonic environment, which suggests dynamically triggered earthquakes could initiate due to multiple physical mechanisms.

The dynamic triggering of $M > 5$ earthquakes is rarely observed beyond the near-field aftershock zone [*Parsons and Velasco*, 2011], but the phenomenon is documented for a few main shocks. One example is the 1992 M5.3 Little Skull Mountain event that occurred 22 h after the 1992 M7.3 Landers main shock in Southern California [*Gomberg and Bodin*, 1994]. The Little Skull Mountain earthquake was the largest dynamically triggered event associated with the 1992 Landers main shock and was preceded by a foreshock sequence that initiated at the time of the Landers event. *Gomberg and Bodin* [1994] report the fault rupture plane was preferentially oriented with respect to the peak dynamic strain of 4 microstrains calculated for the hypocentral depth. A second example is the M5.2 earthquake and an associated earthquake swarm in the Gulf of California that initiated in the hours following the passage of surface waves from the 2011 M9.0 Tohoku main shock [*Gonzalez-Huizar et al.*, 2012]. A third example, and arguably the largest dynamically triggered earthquake, is the 2013 M7.5 Craig, Alaska earthquake that occurred 3 months following the M7.7 Haida Gwaii earthquake [*Gomberg*, 2013]. The final event that had multiple triggered earthquakes is the 2012 M8.6 Indian Ocean earthquake with 6 days of above-average global seismicity for $M \geq 5.5$ earthquakes followed by a 95 day period of global quiescence for $M \geq 6.5$ events [*Pollitz et al.*, 2012, 2014]. The lack of additional observations of dynamic far-field triggering of $M \geq 5$ earthquakes suggests that these larger events are less responsive to transient stress changes [*Parsons et al.*, 2012].

Questions remain regarding large-magnitude earthquakes remotely triggering other $M \geq 5.5$ earthquakes and the delay time for observable changes in earthquake activity [*Gomberg and Sherrod*, 2014; *Pollitz et al.*, 2012]. In this study, we systematically examine global seismicity of $M \geq 5.5$ events in the months following the passage of large-amplitude surface waves at remote distances beyond the aftershock zone for $M \geq 7.5$ main shocks. Our goal is to investigate if a resolvable triggering signal, either immediate or delayed within the first 10 days of the main shock, exists in the catalog records. Additionally, we explore the data for periods of reduced global seismicity following a transient stress, i.e., a dynamic shadowing effect [*Pollitz et al.*, 2014]. This study relies on a systematic approach that examines 113 $M \geq 7.5$ events in 35 years of earthquake catalog data as a collective set and separated by fault mechanism. The techniques of this study allow us to test for periods of enhanced or suppressed activity following a transient stress perturbation by producing rate curves of far-field seismic activity for each main shock.

2. Systematic Catalog Analysis for Delayed Dynamic Triggering

2.1. Terminology

Throughout the paper, we will follow the terminology described here. A $M \geq 7.5$ earthquake is referred to as a main shock, if it did not occur within 2.5 fault lengths and 36 h of a preceding $M \geq 7.5$ event. A preshock is any event occurring before the main shock within the elevated strain region described in section 2.2. Similarly, a postshock is any event occurring during or after passage of the main shock surface waves within the elevated strain region. Here we only consider $M \geq 5.5$ events as preshock and postshock. To note, we do not use aftershock to describe the far-field earthquakes because we are interested in events beyond the region normally associated with that term and postshocks can be larger than the main shock [*Chen et al.*, 2013]. The near field encompasses the region 2.5 fault lengths from a main shock. The far field is the region beyond the near field. Static triggering can produce near-field postshocks. Dynamic triggering is the occurrence of postshocks during the passage of seismic waves. Delayed dynamic triggering can produce a postshock in the days following the passage of seismic waves. Dynamic stress shadowing is a seismic quiescent period following a transient stress.
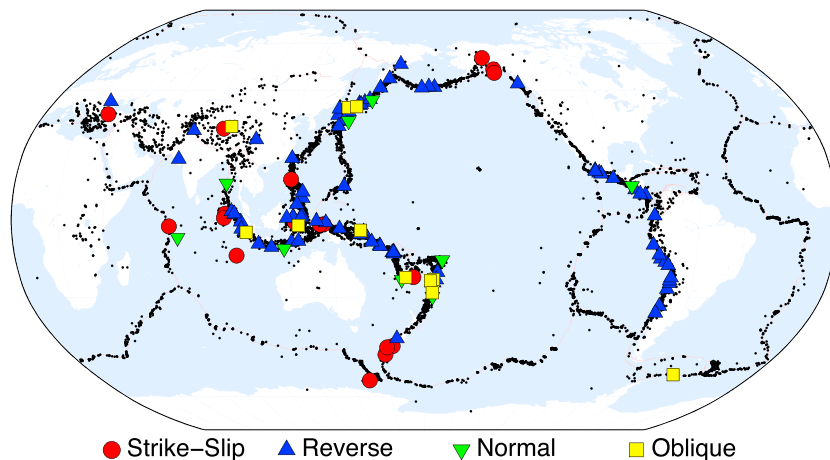
Figure 1. Locations of the 122 $M \geq 7.5$ main shocks and exclusion-zone declustered $M \geq 5.5$ seismicity between 1977 and 2012 in the GCMT catalog. Symbols indicate the fault type determined using the plunge of the compression, tension, and null axis from the GCMT moment tensor solution. Black dots indicate the $M \geq 5.5$ trigger candidates.

2.2. Methods

Our analysis examines only the far-field, $M \geq 5.5$ seismic activity following $M \geq 7.5$ main shocks in a global catalog. We build on the results by *Parsons and Velasco* [2011] that indicate no increase in $5 < M < 7$ events following $M \geq 7$ main shocks at distances greater than 1000 km from the epicenter. We allow for $M \geq 7.5$ events to trigger other large events and stack the seismicity to resolve a possible increase in the 10 days following the main shocks. Our search area is spatially limited, using a model to define the region of elevated dynamic strain that is unique to each main shock. This allows us to consider only far-field activity occurring in regions that are dynamically strained during the passage of seismic waves. We adopt a peak dynamic strain threshold of ≥ 0.1 microstrain (corresponding to a transient stress of ~3 kPa) that has been previously shown to trigger activity in seismically active areas [*Peng et al.*, 2010; *Pollitz et al.*, 2012; *van der Elst and Brodsky*, 2010].

2.2.1. Earthquake Catalog

Data from the Global Centroid Moment Tensor (GCMT) catalog between January 1976 and December 2013 containing 39,989 events were used for the analysis [*Dziewonski et al.*, 1981; *Ekström et al.*, 2012]. The GCMT catalog includes a moment magnitude and the moment tensor solution making it ideal for decomposing the earthquakes by fault mechanism. The magnitude of completeness was calculated using the maximum curvature [*Gutenberg and Richter*, 1944] and maximum likelihood methods [*Aki*, 1965; *Wiemer and Wyss*, 2000], finding a completeness level of $M5.3$ and $M5.7$, respectively. Due to the uncertainty in the magnitude of completeness, we use the average of the two methods, $M5.5$, throughout this study [*Gomberg and Sherrod*, 2014]. The event depth was limited to <100 km, with 77% of the events at a depth less than 35 km. The final catalog contains 12,707 $M \geq 5.5$ earthquakes meeting these criteria for the analysis.

The analysis considers all the 122 $M \geq 7.5$ main shocks from 1977 to 2012 as sources of a transient strain perturbation (Figure 1). Each main shock is assigned a faulting mechanism using the moment tensor solution to calculate the compression (*P*), tension (*T*), and null (*B*) axis plunge. Following *Mallman and Parsons* [2008], the earthquakes are classified with a *T*-axis plunge $\geq 50°$ as reverse events, a *P*-axis plunge $\geq 60°$ as normal events, and a *B*-axis plunge $\geq 60°$ as strike-slip events. All remaining events were classified as oblique. This allows the main shocks to be characterized by mechanism for separate analyses. The time frame considered is a ± 1 year window of cataloged seismicity around each main shock in order to represent the natural variability in earthquake occurrence. Main shock sequences are removed from the catalog if multiple $M \geq 7.5$ earthquakes are present within 36 h of the original main shock and within 2.5 fault lengths. When removing main shocks, the largest earthquake in the sequence is kept for the analysis. This allows the removal of rapid sequences of main shocks such as the 2011 $M9.0$ Tohoku-Oki and the two $M \geq 7.5$ aftershocks that occurred within 1 h. Similarly, the 36 h time window removes main shock clusters like the 2000 Papua New Guinea earthquake sequence of three $M \geq 7.5$ main shocks that occurred within 35 h [*Park and Mori*, 2007]. In total, this procedure removes nine $M \geq 7.5$ earthquakes and leaves 113 $M \geq 7.5$ main shocks (see the supporting information for catalog).
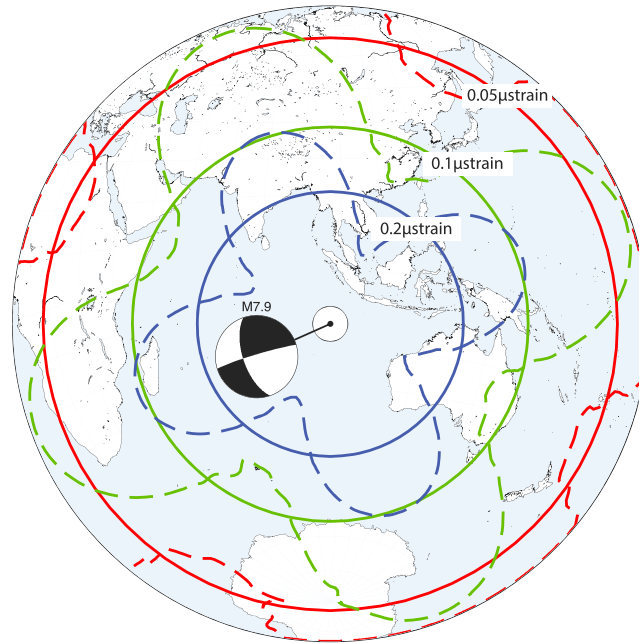
Figure 2. Extent of dynamically strained region calculated for the 18 June 2000 $M7.9$ earthquake in the Indian Ocean using the empirically derived shear-strain values (solid circles) from the magnitude and the modeled strain from synthetic waveforms (dashed lines). Shown are three regions of peak dynamic strain calculated for 0.2 (blue), 0.1 (green), and 0.05 microstrain (red). The modeled strain amplitudes are the square root of the second invariant of the deviatoric strain tensor obtained from a point-source model of surface waves generated by the event, using the focal mechanism shown from the GCMT catalog. The inner exclusion zone extends 2.5 rupture lengths from the epicenter to a distance of ~500 km and is represented as a white disk centered on the main shock. For each main shock, all events from the exclusion-zone declustered catalog in the high-strain region for ±1 year are used to produce the rate curves.

2.2.2. Declustering

We avoid using a declustering method that requires fitting multiple model parameters; instead, we implement an exclusion-zone method for each main shock in the catalog [*Gomberg and Sherrod*, 2014; *Pollitz et al.*, 2012; *Shearer and Stark*, 2012]. The radial exclusion zone extends 2.5 characteristic fault lengths from each main shock, calculated using the fault type and magnitude [*Wells and Coppersmith*, 2013], and removes all near-field events for a period of 1 year following all $M \geq 7.5$ main shocks. The exclusion method is repeated for the $5.5 \leq M \leq 7.5$ catalog, removing earthquakes in the exclusion zone of each event within 24 h and applying a minimum distance of 100 km while keeping the first. The exclusion-zone declustering method removes 1849 near-field events for all main shocks and 1046 far-field events leaving 9812 events for the analysis (see the supporting information for catalog).

2.2.3. Defining Spatial Regions

Seismicity is selected from a spatial region of high dynamic strain determined for each main shock, which is defined by an annulus centered at the epicenter of the main shock that is scaled by the magnitude (Figure 2). The far-field region of interest is restricted to locations where surface waves are the primary source of a transient strain. The inner limit is 2.5 fault lengths, as previously determined during the declustering procedure. The distal limit of the search area is calculated for each main shock using the minimum wave amplitude that corresponds to an estimated strain [*van der Elst and Brodsky*, 2010] with a threshold of 0.1 microstrain (equations (1) and (2)).

$$\varepsilon \approx \frac{V}{C} \approx \frac{A_{max} 2\pi}{C\,T} \tag{1}$$

$$\log_{10} A_{max} = M_S - 1.66 \log_{10}(\Delta) - 2 \tag{2}$$

Here V is particle velocity, C is wave velocity, A_{max} is maximum displacement in micrometers, T is dominant period in seconds, M_S is surface wave magnitude, and Δ is distance [*Lay and Wallace*, 1995]. The strain is estimated from equation (1) using the amplitude as a function of distance and magnitude, as described in equation (2). This study assumes a surface wave velocity of 3.5 km/s and a dominant period of 20 s. These are representative parameters for Rayleigh waves [*Lay and Wallace*, 1995]. As noted by *van der Elst and Brodsky* [2010], if the Love wave results in the largest surface displacement, the assumptions for equation (1) can overestimate the maximum strain by ~20% if a constant period of 20 s is assumed. Assuming representative elastic moduli for the lithosphere (shear modulus of 30 GPa, Poisson's ratio of 0.25), this corresponds to a shear stress transient of about 3 kPa, an order of magnitude greater than stress perturbation that induces nonvolcanic tremor [*Thomas et al.*, 2009].

2.2.4. Synthetic Waveform Strain Calculation

The empirical values obtained from equations (1) and (2) do not consider the spatial pattern of dynamic strain and represent an estimated peak strain for a given distance. We complement the strain calculation from
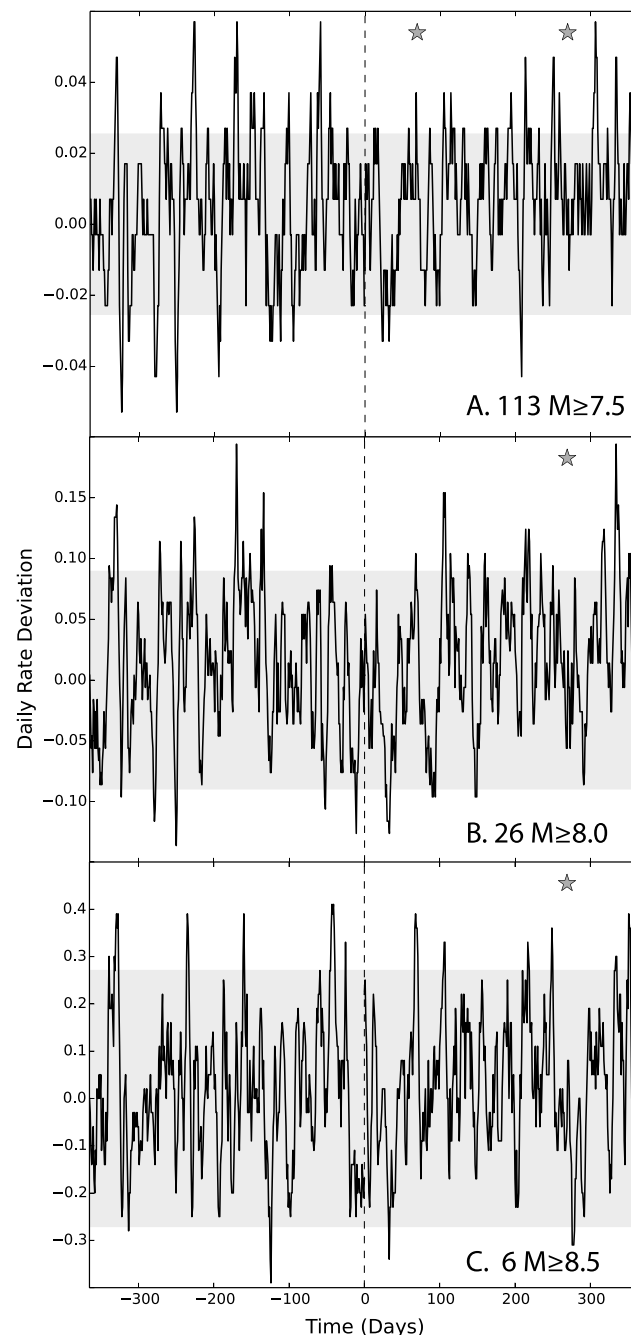
Figure 3. Stacked seismicity rate curves of exclusion-zone declustered $M \geq 5.5$ events in the region of elevated strain (≥ 0.1 microstrain from equations (1) and (2)) for populations of main shocks with different magnitude ranges, with time zero relative to each main shock. The curve indicates the deviation from the normalized background rate for the population using a moving average with a 1 day step and 3 day half width. The gray shading represents the 95% confidence interval calculated using only events within the defined high-strain region during a 2 year period prior to the main shock. Stars indicate the occurrence of a $M \geq 7.5$ main shock in the elevated strain area when calculating the rate curve. Pulses of activity, as well as brief periods of low activity, exist throughout the 2 year period but do not correlate with the timing of the main shock. The stacked rate curves for (a) 113 $M \geq 7.5$ main shocks between 1977 and 2012, (b) 26 $M \geq 8.0$ main shocks, and six $M \geq 8.5$ events.

equations (1) and (2) by modeling the expected displacements for a select group of main shocks and the associated shear strain magnitude and duration. Seismic waves are modeled with a direct Green's function method using an isotropic preliminary reference Earth model (PREM) on a symmetric sphere [*Friederich and Dalkolmo*, 1995; *Pollitz*, 1996; *Pollitz et al.*, 2012]. Synthetic waveforms are produced using a point source solution at 5150 node points evenly spaced around the surface of the planet [*Pollitz et al.*, 2012]. The main shock moment solution, half width of the rate function, and the strike, rake, and dip of the fault plane from the GCMT catalog are used for the model calculation. The choice of nodal plane does not alter the solution and we use the parameters from the first nodal plane listed in the catalog. We treat each main shock as a far-field point source and only consider the long-wavelength displacement. The shearing magnitude is estimated from the square root of the second invariant of the deviatoric strain tensor for each synthetic seismogram and should be considered an upper limit for the transient strain [*Jaeger et al.*, 2007]. The long-period synthetic seismograms are filtered to the GCMT half-duration time when calculating the strain field time series. The strain duration represents the time, in seconds, above the strain threshold for each node point. The dashed contour line in Figure 2 illustrates the extent of the peak dynamic shear-strain field for an 18 June 2000 $M7.9$ strike-slip event in the southern Indian Ocean (13.47°S, 97.17°E) using a threshold of 0.05, 0.1, and 0.2 microstrain. Included in Figure 2 is the radial extent of the empirical strain calculation determined using equations (1) and (2) shown with solid lines. We verify the results using data from the station CTAO to compare with the synthetic seismograms (Figure S1).

2.2.5. Rate Curves

We calculate the daily rate of seismicity for a ±365 day period for each main shock using the $M \geq 5.5$ declustered catalog. The procedure is applied to all preshock and postshock in the dynamic-triggering target region of all 113 $M \geq 7.5$ main
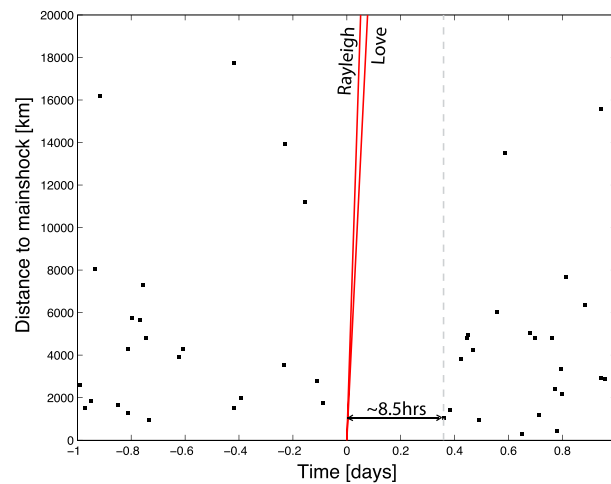
Figure 4. Seismicity ($M \geq 5.5$) for ±1 day relative to the 113 $M \geq 7.5$ stacked main shocks. The red lines indicate the arrival time of the Love and Rayleigh waves. The times of the $M \geq 5.5$ events shown are relative to the associated main shock and events are selected from the declustered far-field preshock and postshock. The first event is a $M5.8$ that occurs ~8.5 h after and ~1050 km away from the 1991 $M7.6$ main shock located offshore Costa Rica.

shocks and stacked as a whole and by fault mechanism. Curves are constructed using a moving average with a 1 day time step and 3 day half width. Pre-main shock events are summed for the discrete time t_{before} using a bin width of $[t_{before} - 3$ days, $\min(0, t_{before} + 3$ days$)]$. Post-main shocks events are summed for the discrete time t_{after} using a bin width $[\max(t_{after} - 3$ days, $0)$, $t_{after} + 3$ days$]$. The rate is scaled to the correct bin width for every discrete time interval. This avoids averaging across time zero and ensures a separation between preshock and postshock when calculating the daily rate [*Pollitz et al.*, 2012]. The rate curves are stacked with time zero relative to each main shock and normalized by the total number of main shocks. We use a lower magnitude cutoff for main shocks of $M7.5$, $M8.0$, and $M8.5$. The background rate is determined using a Monte Carlo procedure that randomizes the event times in the catalog and perturbs each location by up to 50 km [*Parsons and Velasco*, 2011]. This simulated catalog approach allows us to retain the spatial and temporal characteristics of the original catalog that are needed for the scaling used in our analysis. For each event a rate curve is produced using a simulated catalog for 2 years prior to the main shock. The process is repeated 200 times and the background rate and confidence intervals are obtained from the distribution of rate curves.

2.3. Results

2.3.1. All Fault Types

For an observable delayed seismic response in the far field, either an increase or decrease in activity, we need a large population of main shocks that contains multiple fault orientations and varying environments. Figure 3 shows the normalized daily rate curves stacked for the 113 $M \geq 7.5$, 26 $M \geq 8.0$, and 6 $M \geq 8.5$ main shocks with time zero relative to each main shock origin time. Since we are using a subset of declustered $M \geq 5.5$ events for each main shock, the rate curves represent the deviation in seismic activity and are reduced by the calculated background rate. The 95% confidence bounds are shown in gray. Periods of increased activity appear as peaks in the rate that occasionally exceed the 95% confidence interval. An increase in postshock activity above the 95% level is not observed for at least 10 days after time zero for the three magnitude thresholds shown in Figure 3. We do not consider later pulses of activity as evidence for a systematic increase in far-field seismicity.

The first postshock in the $M \geq 7.5$ stacked rate curves occurs ~8.5 h following the main shock (Figure 4). The $M5.8$ postshock is located ~1050 km from the 1991 $M7.6$ main shock that occurred offshore from Costa Rica. No evidence for immediate triggering of $M \geq 5.5$ postshocks is observed in our study. Additionally, our results do not indicate a dynamic shadowing effect following the main shocks. The results do indicate a subtle increase in daily rates but changes in activity are not outside the statistical confidence intervals.

2.3.2. Main Shocks by Fault Type

The main shocks are separated by fault type and rate curves are produced in order to test if a particular main shock faulting mechanism results in observable changes. The motivation for this separation is the difference in radiation pattern and dominant surface wave associated with differing fault mechanisms. The decomposition produces similar distributed pulses in activity above the 95% confidence level as are observed in the initial combined set of main shocks. Figure 5 contains the rate curves for the $M \geq 7.5$ main shock decomposed into 17 strike-slip, 77 reverse, 8 normal, and 11 oblique events. Figure 5a shows the strike-slip events, which indicates a sharp increase in daily rate following the main shock. This increase in the rate curve immediately after the main shock is strongly influenced by the 2012 $M8.6$ Indian Ocean event, which is shown to have increased global
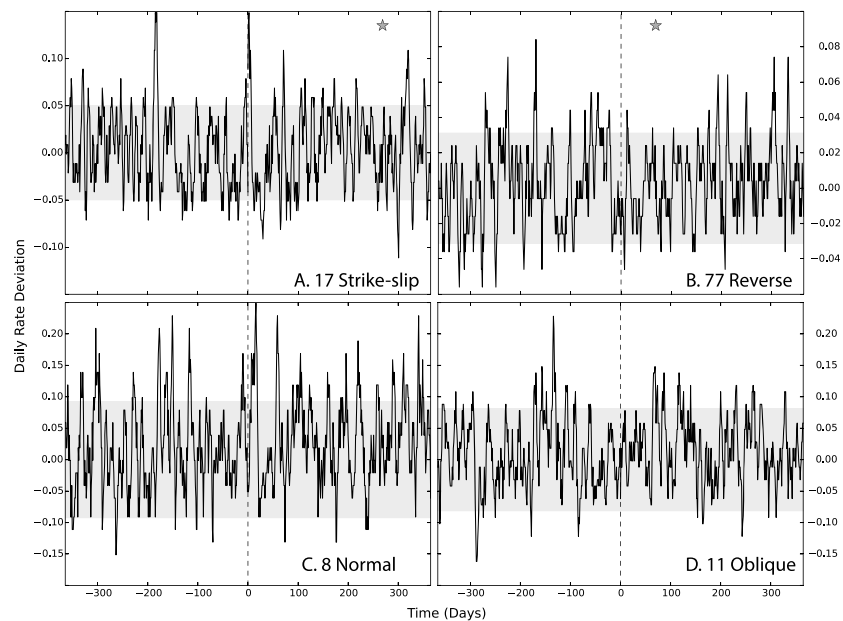
Figure 5. The 113 $M \geq 7.5$ main shocks are separated by fault type and $M \geq 5.5$ exclusion-zone declustered seismicity is stacked to produce rate curves. Shown is the deviation from background rates with the 95% confidence interval in gray. Stars indicate the occurrence of a $M \geq 7.5$ main shock in the circular ≥ 0.1 microstrain area calculated from equations (1) and (2). The strike-slip and normal main shocks indicate a period of elevated seismicity during the first 10-days following the main shock. The elevated seismicity rate following strike-slip main shocks is dominated by the 2012 $M8.6$ Indian Ocean main shock. As shown in Figure 6 the rate increase during the first 10 day period is not present when the 2012 main shock is removed from the rate curve. The increase following the normal main shocks is attributed to the 1977 $M8.3$ main shock.

seismicity for 10 days [*Pollitz et al.*, 2012]. Also evident in the strike-slip rate curve is a period of activity below the confidence interval from days 25 to 33 after the main shock. The reverse events (Figure 5b) indicate a 3 day increase in activity 12 days after the main shock. No sustained decrease in activity is observed for the reverse main shocks. The normal main shocks in Figure 5c indicate an increase in seismicity that initiates 4 days after the main shocks and continues for 20 days. The observed increase following the normal main shocks appears to be dominated by a rate increase following the 1977 $M8.3$ event in the southern Indian Ocean. The oblique main shocks (Figure 5d) do not produce a resolvable increase or decrease in activity following the main shocks. When stacking only the largest main shocks, we are increasing the extent of the region of elevated strain but sampling with fewer main shocks to support any observation. The rate curves for the 26 $M \geq 8.0$ main shocks produced using equations (1) and (2) are separated by fault type and shown in Figure S2. The rate curves contain 4 strike-slip, 16 reverse, 3 normal, and 3 oblique main shocks. We observe similar rate increases for the strike-slip and normal fault types that are sustained for 10 and 21 days, respectively.

2.3.3. Strain Field Derived From Synthetic Waveforms

To further test the significance of the possible far-field increase in seismicity following the strike-slip main shocks, we calculate a global strain field using synthetic seismograms derived from the GCMT moment tensor solution for the 17 strike-slip, 3 $M \geq 8$ normal, and 5 $M \geq 8.5$ reverse main shocks. We are redefining the elevated strain field from the original circular region determined using equations (1) and (2) and use the modeled shear-strain magnitude and duration to represent a strain field based on the seismic radiation pattern. The computed strain field (≥ 0.1 microstrain) includes a larger region defined by the radiation pattern of the focal mechanism (Figure 2). The rate curves for the strike-slip main shocks using the redefined strain field are shown in Figure 6. The modeled strain field increases the number of events in the far field of the 17 strike-slip main shocks by 429 for a total of 3004 earthquakes. We investigate the influence of the 2012 $M8.6$ Indian Ocean earthquake on the analysis and find ~20% of the 3004 events used to produce the rate curve in Figure 6a are associated with the 2012 event. The elevated seismicity is clearly observed in the top panels of Figure 6 for the $M7.5$ and $M8.0$ magnitude thresholds, consistent with the results shown in Figures 5a and S2a. The analysis is repeated with the 2012 $M8.6$ Indian Ocean main shock removed and the results are shown in Figures 6c and 6d where the elevated seismicity is no longer observable. Similar steps
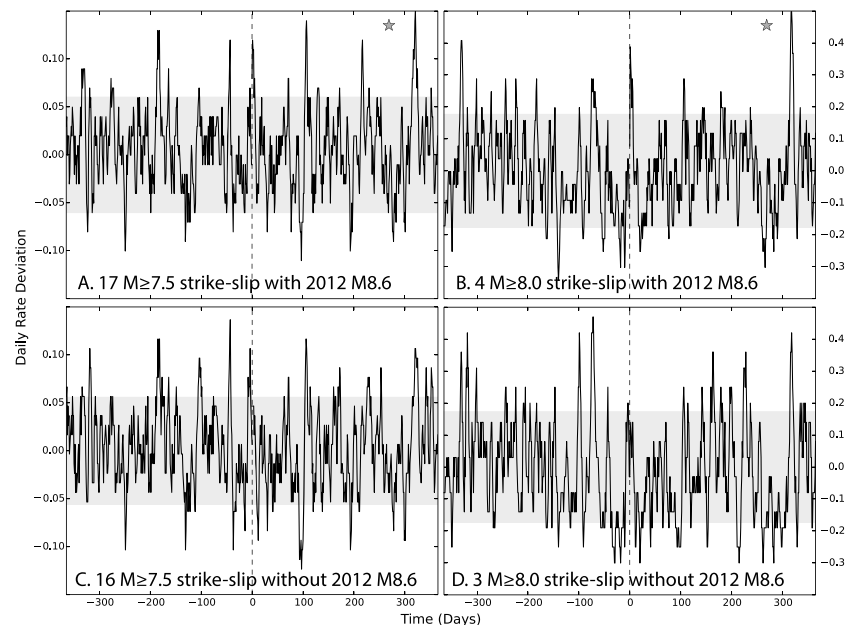
Figure 6. Seismicity rate curves for $M \geq 5.5$ events in the region of elevated strain (>0.1 microstrain) for strike-slip events calculated using the synthetic waveforms. The strike-slip main shock rate curves illustrate the influence of the 2012 $M8.6$ Indian Ocean main shock and its associated elevated remote seismicity. (a, b) Observed deviation of $M \geq 5.5$ event rates in the high-strain search areas for each main shock including the 2012 $M8.6$ Indian Ocean earthquake for $M \geq 7.5$ and $M \geq 8$ strike-slip events. (c, d) Rate variations with the 2012 $M8.6$ Indian Ocean main shock removed from the catalog. No increase during the first 10 days above the confidence interval is observed when performing this test at the $M \geq 7.5$ and $M \geq 8.0$ thresholds.

were taken to produce and stack rate curves for the normal main shocks that indicate elevated rates. The increase is found to be due to activity following the 1977 $M8.3$ main shock in the southern Indian Ocean.

3. Discussion

3.1. Findings and Comparison With Prior Results

We focus our study on the remote triggering of $M \geq 5.5$ earthquakes and analyze the data for a systematic change in earthquake rates rather than focusing on single postshocks as potential triggered candidates. Our results indicate no immediate far-field triggering of $M \geq 5.5$ and are consistent with *Parsons and Velasco* [2011] who do not find immediate triggering of $5 < M < 7$ events at distances greater than 2–3 rupture lengths following 205 $M \geq 7$ main shocks. Our findings show that the first $M \geq 5.5$ postshock occurs ~8.5 h following the passage of seismic waves (Figure 4). A suppression of earthquake rates is also not observed in the $M \geq 7.5$ rate curves shown in Figures 3 and 5. For the $M \geq 8.0$ strike-slip main shocks, rate curves shown in Figure 6 indicate a period of reduced seismicity from 20 to 23 days following the main shock. Similar periods of reduced activity are also present in the months before and well after the main shock and may represent natural fluctuations in seismicity. While the period of enhanced seismicity after the 2012 $M8.6$ Indian Ocean earthquake was followed by an unusual 95 day long absence of $M \geq 6.5$ events [*Pollitz et al.*, 2014], we do not find a corresponding systematic reduction of $M \geq 5.5$ events.

Recent studies have suggested that the largest $M \geq 8.5$ main shocks are capable of producing an increase in global seismicity [*Pollitz et al.*, 2012]. We test this by exploring main shock magnitude ranges above $M7.5$, $M8.0$, and $M8.5$ and find that observable rate changes are associated only with a few individual main shocks. As noted by *Pollitz et al.* [2012], the 2 day rate increase following the five largest subduction events is less than the increase following the 2012 $M8.6$ Indian Ocean main shock. Figure 3c includes the five largest subduction events and the 2012 $M8.6$ Indian Ocean main shock, which indicates a subtle increase that is difficult to separate from the long-term variability in seismicity and does not exceed the 95% confidence bounds. We also consider the possible role of main shock fault mechanism, which produces different amplitudes and patterns of Rayleigh and Love waves, but do not find substantially different rate curves as a function of

faulting style (Figure 5). By extending the period of seismicity to many months before and after the main shock, we observe the natural fluctuations in $M \geq 5.5$ events and avoid interpreting such background variations as significant rate changes. Several times, the calculated daily rate during the 2 year period exceeds the confidence intervals but is not associated with transient seismic waves. The variability in rate is expected due to the stochastic occurrence of seismic events.

3.2. Target Selection, Data Windowing, and Potential Caveats

A unique feature in our study is the varying spatial window that selects the seismicity rate in regions of the largest dynamic strain. Our spatial scaling method tests the importance of wave amplitude with respect to the triggering potential. The justification of this scaling relationship is to limit the selection of postshocks to far-field regions that experience a substantial transient strain. We calculate rate curves for 113 $M \geq 7.5$ main shocks using strain thresholds of 0.05, 0.1, and 0.2 microstrain and do not find notable differences in the distribution of postshock activity (Figure S3). Therefore, we maintain a strain threshold of 0.1 microstrain for the analysis. One limitation to our method is not considering the receiver fault orientation with respect to a transient strain when selecting possible trigger candidates [*Gonzalez-Huizar and Velasco*, 2011; *Hill*, 2012]. Resolving the Coulomb shear and normal stress changes for each postshock considered would provide a better metric for the triggering potential of a transient strain but is beyond the scope of this study.

The postshock selection process is central to the results presented throughout this study and can be influenced by the preprocessing methods applied to the original set of cataloged earthquakes. Our study limits all main shocks and postshocks to depths <100 km and does not consider main shock-postshock interaction that has been observed in deep-focus earthquake sequences [*Tibi et al.*, 2003]. We implement an exclusion zone that eliminates all postshocks within 2.5 fault lengths of the epicenter in order to avoid the classical aftershock zone produced by both static and dynamic stress changes. Our tests do not indicate a significant change in the results by decreasing the exclusion zone to a factor of 2 or increasing to a factor of 4 of the estimated fault lengths. Reducing the exclusion zone distance below a factor of 2 introduces local aftershocks into the rate curves. We also test the temporal window length for excluding near-field events and observe insignificant rate differences when shortening to a 35 day window from a 1 year window (Figure S4). Similarly, we evaluate rate curves without the far-field declustering of local aftershocks and obtain similar results.

The choice of a magnitude threshold of $M5.5$ represents the completeness of the catalog. Using the more conservative magnitude of completeness of $M5.7$ for the GCMT catalog would reduce the number of events in the selection process. Performing the analysis at the higher magnitude of completeness does not significantly alter the results. Conversely, using events down to $M5.0$ increases the number of events considered and does change the background rate. Calculating rate curves using the lower magnitude threshold does not produce any additional deviations in seismic activity immediately following the transient strain. Therefore, we maintain a threshold of $M5.5$ with regard to the magnitude of completeness calculated. The choice of window width when smoothing the data set can also influence the results. Here the rate curves are smoothed using a 1 day bin with a 3 day half width. Other studies have implemented 1 month windows over restricted spatial subsets [*Gomberg and Sherrod*, 2014] and 1 day windows on global scales [*Pollitz et al.*, 2012]. We tested different windows as short as 1 day and up to 1 month without significant changes to our results (Figure S5).

3.3. Significant Rate Changes

The rate curves indicate significantly elevated rates of far-field seismic activity in the immediate days following only two large main shocks, each with different characteristics. These are the 1977 $M8.3$ normal and the 2012 $M8.6$ strike-slip earthquakes, both located in the Indian Ocean (Figure 7). The 1977 $M8.3$ main shock produced a delayed response on the order of days. The first postshock outside the exclusion zone is a $M5.5$, 2 days after the main shock with the far field not reaching significantly elevated rates until 10 days afterwards followed by about 2 weeks of enhanced activity. This delay time subsequent to the 1977 $M8.3$ is considerably greater than that found for the 2012 M8.6 Indian Ocean main shock, which is followed by four $M \geq 5.5$ postshocks in the first 24 h, the first being a $M6.0$ 14 h after the passage of the seismic waves. *Pollitz et al.* [2012] show the significance of the 2012 $M8.6$ Indian Ocean earthquake triggering with respect to a global background rate. This study does not observe a similar increase when combining 35 years of $M \geq 5.5$ seismicity following 113 large main shocks indicating the uniqueness of the 2012 $M8.6$ Indian Ocean
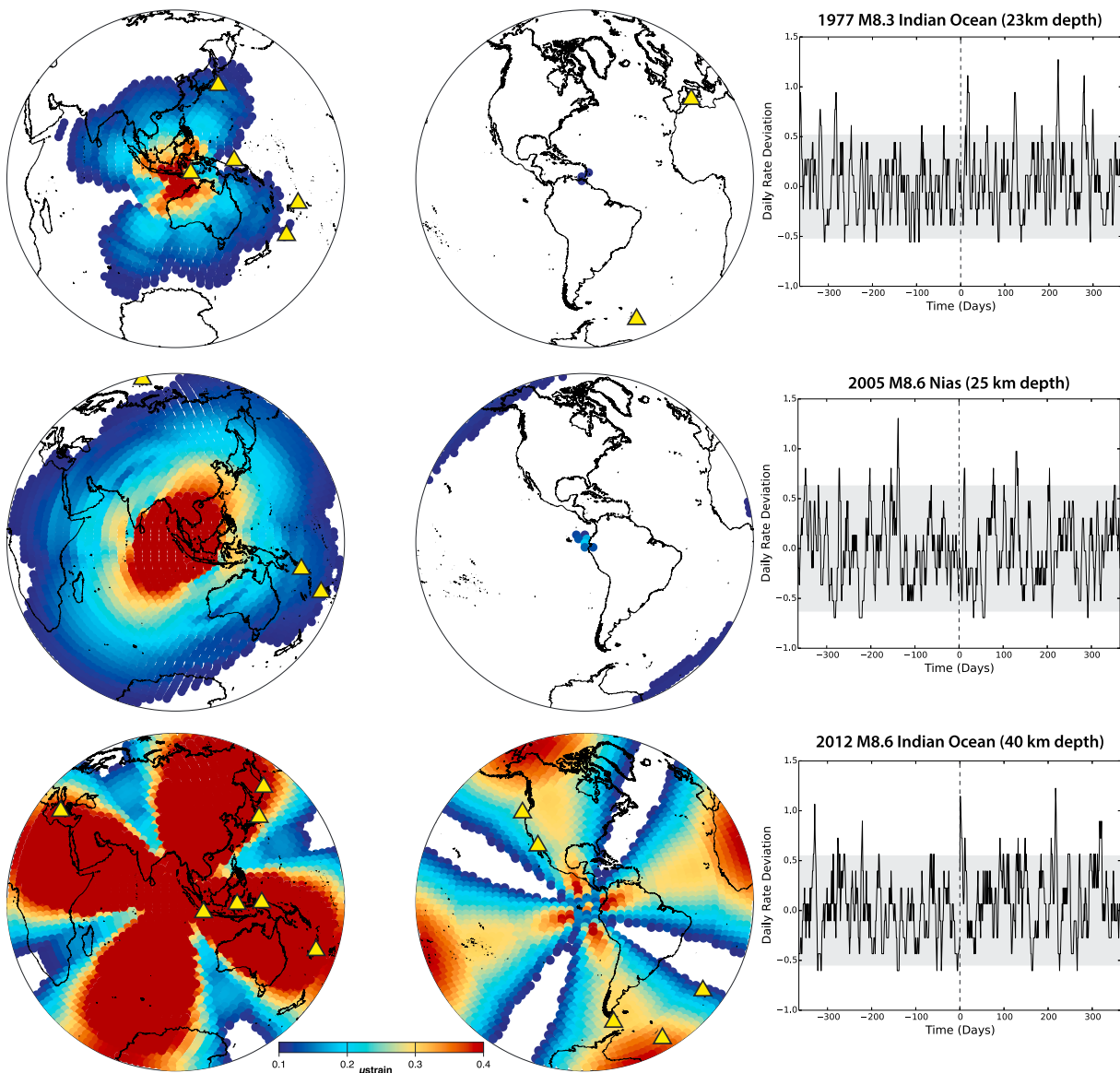
Figure 7. Comparison of modeled shear strain for three $M > 8$ main shocks located in the east Indian Ocean with different magnitudes, centroid depths, and fault mechanisms. The spatial coloring represents the peak shear strain calculated from the square root of the second invariant of the deviatoric strain tensor using the strain time series filtered to 80 s. The color scale is saturated at 0.4 microstrain. Yellow triangles represent the far-field $M \geq 5.5$ seismic events for 10 days following the main shock. To the right is the seismicity rate curve for the modeled event shown to the left. The top panel shows the 1977 $M8.3$ Indian Ocean normal event, the middle panel represents the 2005 $M8.6$ Nias subduction thrust main shock, and the bottom panel is produced using the 2012 $M8.6$ Indian Ocean strike-slip event, with three $M \geq 5.5$ postshocks occurring within 24 h of the main shock.

earthquake. If this earthquake represents a unique occurrence of far-field triggering of $M \geq 5.5$ events, then what are the requirements for a large magnitude earthquake to trigger other large magnitude earthquakes at remote distances?

The 2012 $M8.6$ Indian Ocean earthquake is the largest strike-slip event recorded with modern instrumentation and was composed of a complex rupture sequence breaking deep into the mantle lithosphere [*McGuire and Beroza*, 2012; *Meng et al.*, 2012]. The transient stress during the passage of the surface waves apparently was large enough to advance the earthquake cycle of multiple $M \geq 5.5$ events. The delayed dynamic triggering of postshocks found by *Pollitz et al.* [2012] occurred in regions of >0.2 microstrain lasting more than 100 s during the passage of the surface wave train. We compare the strain duration and seismicity for the 2005 $M8.6$ Nias subduction thrust event and the nearby 2012 $M8.6$ Indian Ocean main shock (Figure 7 and S6). The two main

shocks are separated by ~500 km and the centroid depth of the 2005 $M8.6$ Nias event is 25 km, making it 15 km shallower than the 2012 $M8.6$ Indian Ocean main shock. Figure 7 displays the difference in spatial extent of the elevated strain regions. The far-field $M \geq 5.5$ seismicity of the first 10 days following the two events shown in Figure 7 demonstrates the lack of large events in the much smaller region of prolonged strain for the Nias earthquake. The 2005 $M8.6$ Nias main shock had three $M \geq 5.5$ postshocks, one of which is not within the elevated strain region, whereas the 2012 $M8.6$ Indian Ocean main shock had 11 postshocks all within the region of elevated dynamic strain. We cannot dismiss the postshocks following the 2005 $M8.6$ Nias main shock in the elevated strain region as being triggered even though they do not result in a systematic rate increase.

Frictional instability models using rate-and-state friction parameters indicate a "clock advance" can occur during the passage of seismic waves, but earthquake triggering is possible only if the fault is late in its earthquake cycle [*Gomberg et al.*, 1998]. This leaves the possibility that the 2005 $M8.6$ Nias postshocks' nucleation times were advanced but the delayed occurrence does not produce a distinguishable rate change, which requires multiple postshocks to significantly exceed the expected background rate of large events. A key observation for the multiple postshocks following the 2012 $M8.6$ Indian Ocean main shock is the overlap of Pacific-plate boundaries with the maximum transient strain duration extending to antipodal distances. The combination of multiple critically stressed faults within the plate boundary zone in conjunction with the long duration and large amplitude of transient shaking supports the uniqueness of the 2012 $M8.6$ Indian Ocean global earthquake rate increase.

No immediate triggering of $M \geq 5.5$ earthquakes is observed in this study, which agrees with previous results [*Parsons and Velasco*, 2011], but seems to be in contradiction to the evidence for dynamically triggered microseismicity and nonvolcanic tremor. Using the Guttenberg-Richter relationship and extrapolating results of small-event triggering for 205 $M \geq 7$ main shocks, *Parsons and Velasco* [2011] estimate a total of 25 $M \geq 6.0$ earthquakes are expected to occur within 15 min of the surface waves. Instead, we find that the first $M \geq 5.5$ postshock following the 113 main shocks we consider does not occur until 8.5 h later. *Parsons et al.* [2014] also observed an 8–9 h delay in $M > 5$ earthquakes using a compilation of local catalogs, but no physical explanation exists for this apparent delayed phenomenon. The 2011 $M9.0$ Tohoku main shock did not produce an increase in $M \geq 5.5$ postshocks (Figure S7) but did immediately trigger nonvolcanic tremor and $M \leq 5.0$ postshocks at remote distances [*Chao et al.*, 2013; *Gonzalez-Huizar et al.*, 2012; *Kato et al.*, 2013]. Similarly, the 2002 $M7.9$ Denali, Alaska main shock triggered widespread microseismic activity throughout the western U.S. in regions of low tectonic strain rates indicating that critically stressed faults are present in all tectonic environments [*Gomberg et al.*, 2004]. *Gonzalez-Huizar and Velasco* [2011] and *Tape et al.* [2013] provide unique observations emphasizing the importance of fault orientation with respect to incident seismic waves that trigger low-magnitude earthquakes. Triggered microseismicity is more often observed in extensional or transtensional tectonic environments, with geothermal fields especially responsive to transient deformation, but not all large main shocks trigger remote microseismic activity [*Prejean and Hill*, 2009]. *Parsons et al.* [2012] and *Hill* [2012] show that the stress perturbations on a fault plane occur only for a short duration and the amplitude is dependent on both fault orientation and depth, often reversing during the wave train. The short-lived occurrence of a positive shear stress perturbation may promote smaller magnitude events but does not appear to trigger larger earthquakes. A fundamental puzzle that still remains when observing low-magnitude triggered events is to determine the environmental conditions required for triggered microseismicity to cascade into a $M \geq 5.5$ earthquake.

The lack of evidence for immediately triggering $M \geq 5.5$ events hints at the significance of the delayed occurrence of large-magnitude triggering, resulting in a global rate increase as well as the challenges associated with classifying triggered candidates. *Parsons and Velasco* [2011] also do not observe immediate large magnitude triggering using a magnitude threshold of $M5.5$ and $M6.0$ using the Advanced National Seismic System catalog. Incomplete centroid catalogs during 0.1–0.5 day following a main shock could account for the lack of events [*Iwata*, 2008], but missing earthquakes are typically located in the near field. The first potential triggered candidate in this study occurs ~8.5 h following the main shock (Figure 4). Our results show that the two largest rate increases occur within hours of the 2012 $M8.6$ main shock and 10 days after the 1977 $M8.3$ main shock. The mechanism of delayed dynamic triggering is not well understood and physical models attempting to explain this phenomenon include linear and nonlinear friction models, the redistribution of crustal fluids, and asperity weakening via aseismic deformation [*Harris*, 1998; *Hill and Prejean*, 2007]. Both the nonlinear Coulomb failure and fluid redistribution models require elevated pore pressure at seismogenic depths in order to initiate a time-dependent failure following transient stress [*Brodsky and*

Prejean, 2005; *Parsons*, 2005]. Some frictional failure models also indicate that a transient stress applied late in the fault's seismogenic cycle results in a more significant clock advance toward failure [*Gomberg et al.*, 1998].

One possible weakness in our methodology is the nonuniform times observed for delayed dynamic triggering and the possibility of destructive interference when stacking the time series, thereby not indicating an increase due to the variable time scales that might be involved in delayed triggering. The temporal variation is indicative of a complex nucleation process that may not be represented by a single failure model or initiated uniformly during seismic wave passage. These criteria suggest that only critically stressed faults with elevated pore-pressure conditions are susceptible to a delayed failure subsequent to a transient stress [*Hill and Prejean*, 2007; *Prejean and Hill*, 2009]. An explanation for the rare observations of $M \geq 5.5$ delayed triggering may lie in the occurrence of an ongoing failure process that is augmented by a transient stress, thereby promoting early failure during a multistage nucleation process. This requires that any triggered earthquake be located on a fault that is about to fail in the near future regardless of the external stressing.

3.4. Alternative Approach

In the present study, we have followed the practice usually adopted in triggering studies [*Kane et al.*, 2007; *Parsons and Velasco*, 2011; *Parsons et al.*, 2014], formulating a hypothesis that earthquake triggering is not occurring, then evaluating the significance of actual observations of remote events following a large main shock. We find that when two particular main shocks are excluded, we cannot reject the hypothesis that remote triggering does not occur. It is possible to instead formulate a hypothesis that remote earthquake triggering is occurring, and then evaluate the significance that remote events following a particular large main shock, or composite set of main shocks, are consistent with the hypothesis. An illustrative hypothesis is that the number of remote postshocks (e.g., occurring globally outside a 1000 km exclusion zone) within 6 days following a large main shock is above the average background rate by 10 events, i.e., the excess that actually occurred following the 2012 M8.6 Indian Ocean main shock [*Pollitz et al.*, 2012]. In detail, the target excess number of events would be dependent on main shock magnitude. A probability density function that could be used to test this hypothesis could be obtained by compiling counts of background "remote" seismicity in random 6 day intervals plus 10. It would be possible to perform tests of all post-main shock seismicity examined in the present study with this approach, and it is worthy of future study.

4. Conclusion

We have analyzed 35 years of global $M \geq 7.5$ main shocks to investigate the effect of a transient stress on $M \geq 5.5$ seismicity. The systematic far-field triggering of $M \geq 5.5$ far-field events is not supported by our results and is not preferential to a faulting mechanism. In contrast to frequently observed triggering of microseismicity and tremor, we do not find any $M \geq 5.5$ far-field events triggered during passage of the seismic waves or during the first hours following an event. The 10 day increase in global seismicity following the 2012 M8.6 Indian Ocean earthquake appears to be unique in the global catalog record. Our results do not rule out the possibility of delayed dynamic triggering of some $M \geq 5.5$ events in the far field but we are unable to distinguish possible trigger candidates from background seismicity. We infer that only ruptures that have already advanced in their nucleation process are susceptible to triggering by surface waves from great remote earthquakes and that the short duration of encouraging stress transients may allow for triggering of smaller earthquakes and tremor, but not of large and damaging events. Based on our analysis of global seismicity spanning 35 years, we conclude that there is no evidence for significantly increased global earthquake hazard at greater than 2.5 rupture lengths away from great main shocks.

References

Aiken, C., Z. Peng, and K. Chao (2013), Tremors along the Queen Charlotte Margin triggered by large teleseismic earthquakes, *Geophys. Res. Lett.*, 40, 829–834, doi:10.1002/grl.50220.

Aki, K. (1965), Maximum likelihood estimate of b in the formula log $N = a - bM$ and its confidence limits, *Bull. Earthquake Res.*, 43, 237–239.

Brodsky, E. E., and S. G. Prejean (2005), New constraints on mechanisms of remotely triggered seismicity at Long Valley Caldera, *J. Geophys. Res.*, 110, B04302, doi:10.1029/2004JB003211.

Brodsky, E. E., V. Karakosta, and H. Kanamori (2000), A new observation of dynamically triggered regional seismicity: Earthquakes in Greece following the August, 1999 Izmit, Turkey earthquake, *Geophys. Res. Lett.*, 27(17), 2741–2744, doi:10.1029/2000GL011534.

Chao, K., Z. Peng, H. Gonzalez-Huizar, C. Aiken, B. Enescu, H. Kao, A. A. Velasco, K. Obara, and T. Matsuzawa (2013), A global search for triggered tremor following the 2011 Mw 9.0 Tohoku earthquake, *Bull. Seismol. Soc. Am.*, 103(2B), 1551–1571.

Chen, K. H., R. Bürgmann, and R. M. Nadeau (2013), Do earthquakes talk to each other? Triggering and interaction of repeating sequences at Parkfield, *J. Geophys. Res. Solid Earth*, *118*, 165–182, doi:10.1029/2012JB009486.

Dziewonski, A. M., T. A. Chou, and J. H. Woodhouse (1981), Determination of earthquake source parameters from waveform data for studies of global and regional seismicity, *J. Geophys. Res.*, *86*, 2825–2582, doi:10.1029/JB086iB04p02825.

Ekström, G., M. Nettles, and A. M. Dziewoński (2012), The global CMT project 2004–2010: Centroid-moment tensors for 13,017 earthquakes, *Phys. Earth Planet. Inter.*, *200–201*, 1–9.

Felzer, K. R., and E. E. Brodsky (2005), Testing the stress shadow hypothesis, *J. Geophys. Res.*, *110*, B05S09, doi:10.1029/2004JB003277.

Freed, A. M. (2005), Earthquake triggering by static, dynamic, and postseismic stress transfer, *Annu. Rev. Earth Planet. Sci.*, *33*(1), 335–367.

Friederich, W., and J. Dalkolmo (1995), Complete synthetic seismograms for a spherically symmetric Earth by a numerical computation of the Green's function in the frequency domain, *Geophys. J. Int.*, *122*, 537–550.

Gomberg, J. (2013), Permanently enhanced dynamic triggering probabilities as evidenced by two $M \geq 7.5$ earthquakes, *Geophys. Res. Lett.*, *40*, 4828–4833, doi:10.1002/grl.50933.

Gomberg, J., and P. Bodin (1994), Triggering of the M_s = 5.4 Little Skull Mountain, Nevada, earthquake with dynamic strains, *Bull. Seismol. Soc. Am.*, *84*(3), 844–853.

Gomberg, J., and B. Sherrod (2014), Crustal earthquake triggering by modern great earthquakes on subduction zone thrusts, *J. Geophys. Res. Solid Earth*, *119*, 1235–1250, doi:10.1002/2012JB009826.

Gomberg, J., N. M. Beeler, M. L. Blanpied, and P. Bodin (1998), Earthquake triggering by transient and static deformations, *J. Geophys. Res.*, *103*(B10), 24,411–24,426, doi:10.1029/98JB01125.

Gomberg, J., P. Bodin, K. Larson, and H. Dragert (2004), Earthquake nucleation by transient deformations caused by the M = 7.9 Denali, Alaska, earthquake, *Nature*, *427*(6975), 621–624.

Gonzalez-Huizar, H., and A. A. Velasco (2011), Dynamic triggering: Stress modeling and a case study, *J. Geophys. Res.*, *116*, B02304, doi:10.1029/2009JB007000.

Gonzalez-Huizar, H., A. A. Velasco, Z. Peng, and R. R. Castro (2012), Remote triggered seismicity caused by the 2011, M9.0 Tohoku-Oki, Japan earthquake, *Geophys. Res. Lett.*, *39*, L10302, doi:10.1029/2012GL051015.

Gutenberg, R., and C. F. Richter (1944), Frequency of earthquakes in California, *Bull. Seismol. Soc. Am.*, *34*, 631–644.

Harris, R. A. (1998), Introduction to special section: Stress triggers, stress shadows, and implications for seismic hazard, *J. Geophys. Res.*, *103*(B10), 24,347–24,358, doi:10.1029/98JB01576.

Harris, R. A., and R. J. Archuleta (1991), Fault steps and the dynamic rupture process: 2-D numerical simulations of a spontaneously propagating shear fracture, *Geophys. Res. Lett.*, *18*(5), 893–896, doi:10.1029/91GL01061.

Hill, D. P. (2012), Dynamic stresses, coulomb failure, and remote triggering–Corrected, *Bull. Seismol. Soc. Am.*, *102*(6), 2313–2336.

Hill, D. P., and S. G. Prejean (2007), 4.09 - Dynamic triggering, in *Treatise on Geophysics*, edited by G. Schubert, pp. 257–291, Elsevier, Amsterdam.

Hill, D. P., et al. (1993), Seismicity remotely triggered by the magnitude 7.3 Landers, California, earthquake, *Science*, *260*(5114), 1617–1623.

Husker, A. L., and E. E. Brodsky (2004), Seismicity in Idaho and Montana triggered by the Denali fault earthquake: A window into the geologic context for seismic triggering, *Bull. Earthquake Res.*, *94*(6B), S310–S316.

Iwata, T. (2008), Low detection capability of global earthquakes after the occurrence of large earthquakes: Investigation of the Harvard CMT catalogue, *Geophys. J. Int.*, *174*(3), 849–856.

Jaeger, J. C., N. G. W. Cook, and R. W. Zimmerman (2007), *Fundamentals of Rock Mechanics*, 4th ed., Blackwell, Malden, Mass.

Kane, D. L., D. Kilb, A. S. Berg, and V. G. Martynov (2007), Quantifying the remote triggering capabilities of large earthquakes using data from the ANZA Seismic Network catalog (southern California), *J. Geophys. Res.*, *112*, B11302, doi:10.1029/2006JB004714.

Kato, A., J. I. Fukuda, and K. Obara (2013), Response of seismicity to static and dynamic stress changes induced by the 2011 M9.0 Tohoku-Oki earthquake, *Geophys. Res. Lett.*, *40*, 3572–3578, doi:10.1002/grl.50699.

Lay, T., and T. C. Wallace (1995), *Modern Global Seismology*, Academic Press, San Diego, Calif.

Mallman, E. P., and T. Parsons (2008), A global search for stress shadows, *J. Geophys. Res.*, *113*, B12304, doi:10.1029/2007JB005336.

McGuire, J. J., and G. C. Beroza (2012), A rogue earthquake off Sumatra, *Science*, *336*(6085), 1118–1119.

Meng, L., J. P. Ampuero, J. Stock, Z. Duputel, Y. Luo, and V. C. Tsai (2012), Earthquake in a maze: Compressional rupture branching during the 2012 M(w) 8.6 Sumatra earthquake, *Science*, *337*(6095), 724–726.

Pankow, K. L., W. J. Arabasz, J. C. Pechmann, and S. J. Nava (2004), Triggered seismicity in Utah from the 3 November 2002 Denali fault earthquake, *Bull. Seismol. Soc. Am.*, *94*(6B), S332–S347.

Park, S.-C., and J. Mori (2007), Triggering of earthquakes during the 2000 Papua New Guinea earthquake sequence, *J. Geophys. Res.*, *112*, B03302, doi:10.1029/2006JB004480.

Parsons, T. (2002), Global Omori law decay of triggered earthquakes: Large aftershocks outside the classical aftershock zone, *J. Geophys. Res.*, *107*(B9), 2199, doi:10.1029/2001JB000646.

Parsons, T. (2005), A hypothesis for delayed dynamic earthquake triggering, *Geophys. Res. Lett.*, *32*, L04302, doi:10.1029/2004GL021811.

Parsons, T., and A. A. Velasco (2011), Absence of remotely triggered large earthquakes beyond the main shock region, *Nat. Geosci.*, *4*(5), 312–316.

Parsons, T., J. O. Kaven, A. A. Velasco, and H. Gonzalez-Huizar (2012), Unraveling the apparent magnitude threshold of remote earthquake triggering using full wavefield surface wave simulation, *Geochem. Geophys. Geosyst.*, *13*, Q06016, doi:10.1029/2012GC004164.

Parsons, T., M. Segou, and W. Marzocchi (2014), The global aftershock zone, *Tectonophysics*, *618*, 1–34.

Peng, Z., J. E. Vidale, A. G. Wech, R. M. Nadeau, and K. C. Creager (2009), Remote triggering of tremor along the San Andreas Fault in central California, *J. Geophys. Res.*, *114*, B00A06, doi:10.1029/2008JB006049.

Peng, Z., D. P. Hill, D. R. Shelly, and C. Aiken (2010), Remotely triggered microearthquakes and tremor in central California following the 2010 Mw 8.8 Chile earthquake, *Geophys. Res. Lett.*, *37*, L24312, doi:10.1029/2010GL045462.

Peng, Z., C. Wu, and C. Aiken (2011), Delayed triggering of microearthquakes by multiple surface waves circling the Earth, *Geophys. Res. Lett.*, *38*, L04306, doi:10.1029/2010GL046373.

Pollitz, F. F. (1996), Coseismic deformation from earthquake faulting on a spherical earth, *Geophys. J. Int.*, *125*, 1–14.

Pollitz, F. F., and M. J. S. Johnston (2006), Direct test of static stress versus dynamic stress triggering of aftershocks, *Geophys. Res. Lett.*, *33*, L15318, doi:10.1029/2006GL026764.

Pollitz, F. F., R. S. Stein, V. Sevilgen, and R. Burgmann (2012), The 11 April 2012 east Indian Ocean earthquake triggered large aftershocks worldwide, *Nature*, *490*(7419), 250–253.

Pollitz, F. F., R. Burgmann, R. S. Stein, and V. Sevilgen (2014), The profound reach of the M8.6 11 April 2012 Indian Ocean earthquake: Short-term global triggering followed by a longer-term global shadow, *Bull. Seismol. Soc. Am.*, *104*(2), 972–984, doi:10.1785/0120130078.

Prejean, S. G., and D. P. Hill (2009), Dynamic triggering of earthquakes, in *Encyclopedia of Complexity and Systems Science*, edited by R. Meyers, pp. 2600–2621, Springer, New York.

Prejean, S. G., D. P. Hill, E. E. Brodsky, S. E. Hough, M. J. S. Johnston, S. D. Malone, A. M. Oppenheimer, A. M. Pitt, and K. B. Richards-Dinger (2004), Remotely triggered seismicity on the United States West Coast following the Mw 7.9 Denali fault earthquake, *Bull. Seismol. Soc. Am.*, *94*(6B), S348–S359.

Reasenberg, P. A., and R. W. Simpson (1992), Response of regional seismicity to the static stress change produced by the Loma Prieta earthquake, *Science*, *255*(5052), 1687–1690.

Richards-Dinger, K., R. S. Stein, and S. Toda (2010), Decay of aftershock density with distance does not indicate triggering by dynamic stress, *Nature*, *467*(7315), 583–586.

Rybicki, K., T. Kato, and K. Kasahara (1985), Mechanical interaction between neighboring active faults - Static and dynamic stress-field induced by faulting, *Bull. Earthquake Res. Inst. Tokyo*, *60*, 1–21.

Shearer, P. M., and P. B. Stark (2012), Global risk of big earthquakes has not recently increased, *Proc. Natl. Acad. Sci. U.S.A.*, *109*(3), 717–721.

Stein, R. S. (1999), The role of stress transfer in earthquake occurrence, *Nature*, *402*, 604–609.

Tape, C., M. West, V. Silwal, and N. Ruppert (2013), Earthquake nucleation and triggering on an optimally oriented fault, *Earth Planet. Sci. Lett.*, *363*, 231–241.

Thomas, A. M., R. M. Nadeau, and R. Burgmann (2009), Tremor-tide correlations and near-lithostatic pore pressure on the deep San Andreas fault, *Nature*, *462*(7276), 1048–1051.

Tibi, R., D. A. Wiens, and H. Inoue (2003), Remote triggering of deep earthquakes in the 2002 Tonga sequences, *Nature, 424*(6951), 921–925.

van der Elst, N. J., and E. E. Brodsky (2010), Connecting near-field and far-field earthquake triggering to dynamic strain, *J. Geophys. Res.*, *115*, B07311, doi:10.1029/2009JB006681.

Velasco, A. A., S. Hernandez, T. Parsons, and K. Pankow (2008), Global ubiquity of dynamic earthquake triggering, *Nat. Geosci.*, *1*(6), 375–379.

Wessel, P., W. H. F. Smith, R. Scharroo, J. F. Luis, and F. Wobbe (2013), Generic mapping tools: Improved version released, *Eos Trans. AGU, 94*, 409–410.

Wiemer, S., and M. Wyss (2000), Minimum magnitude of completeness in earthquake catalogs: Examples from Alaska, the Western United States, and Japan, *Bull. Seismol. Soc. Am.*, *90*(4), 859–869.